Pre- and post-irradiation performance of CMS 3D silicon pixel detectors

A. Krzywda[a]*, **E. Alagoz**[a], **M. Bubna**[a], **M. Obertino**[b,d], **A. Solano**[c,d], **K. Arndt**[a], **M. Boscardin**[f], **G. F. Dalla Betta**[g], **L. Uplegger**[e], **J. Ngadiuba**[h], **R. Rivera**[e], **D. Menasce**[h], **L. Moroni**[h], **S. Terzo**[h], **I. Osipenkov**[j], **A. Prosser**[e], **J. Andreson**[e], **S. Kwan**[e], **C.M. Lei**[e], **D. Bortoletto**[a], **G. Bolla**[a], **I. Shipsey**[a], **P. Tan**[e], **N. Tran**[e], **J. Chramowicz**[e], **J. Cumalat**[i], **L. Perera**[l], **M. Povoli**[g], **and A. Vilela Pereira**[k], **R. Brosius**[a], **A. Kumar**[e], **S. Wagner**[i], **F. Jensen**[i], **S. Bose**[m]

[a] *Physics Department, Purdue University, West Lafayette, IN 47907-2036, USA*

[b] *Universit del Piemonte Orientale, Novara, Italy*

[c] *Universit di Torino, Torino, Italy*

[d] *INFN, Sezione di Torino, Torino, Italy*

[e] *Fermilab, Batavia, IL 60510-5011, USA*

[f] *Centro per Materiali e i Microsistemi Fondazione Bruno Kessler (FBK),Trento, Via Sommarive 18, I-38123 Povo di Trento (TN), Italy*

[g] *INFN Padova (Gruppo Collegato di Trento) Dipartimento di Ingegneria e Scienza dell'Informazione, Universit di Trento, Via Sommarive 14, I-38123 Povo di Trento (TN), Italy*

[h] *Universit di Milano-Bicocca, Milan, Italy*

[i] *University of Colorado-Boulder, Boulder, Colorado*

[j] *Texas A&M University, College Station, Texas*

[k] *Instituto di Fisica, Universidade do Estado do Rio de Janeiro (UERJ), Rua Sao Francisco Xavier, 524, 20550-013 Rio de Janeiro, RJ, Brazil*

[l] *University of Mississippi, Department of Physics and Astronomy, University, MS 38677, USA*

[m] *University of Nebraska-Lincoln, Lincoln, NE 68508*

E-mail: `akrzywda@purdue.edu`

ABSTRACT: In preparation for the tenfold luminosity upgrade of the Large Hadron Collider (the HL-LHC) around 2020, three-dimensional (3D) silicon pixel detectors are being developed as a radiation-hard candidate to replace the planar detectors currently being used in the CMS pixel detector. Here we present pre- and post-irradiation test results for 3D detectors. The maximum fluence applied is 3.5×10^{15} n_{eq}/cm^2.

---

*Corresponding author

Contents

1. Introduction

Radiation-hard tracking detectors are being developed for Large Hadron Collider (LHC) experiments to withstand increased radiation from the High-Luminosity LHC (HL-LHC) upgrade (Phase II), to take place around 2020. The detectors currently in use in the innermost barrel layer of the CMS pixel tracker will collect fluences up to the order 10^{15} n_{eq}/cm^2 in their lifetime. After the HL-LHC upgrade, the new detectors in this layer are estimated to receive ten times this amount [1]. The current planar pixel sensors are not designed to withstand this amount of radiation [2]. Three-dimensional (3D) silicon pixel detectors are a promising radiation-hard alternative [3].

3D sensors possess cylindrical electrodes that pass vertically through the bulk. This technology was first introduced in 1997 [4], and has the advantage that electrode distance is independent from substrate thickness 1. This creates many superior features: higher electric fields between the electrodes means lower depletion voltages, shorter charge carrier drift distance speeds up charge collection and increases radiation hardness, and signal efficiency increases because of shorter inter-electrode distance. The drawbacks of 3D technology are: complex processing procedures, increased noise due to high pixel capacitance, and lower efficiency in some low-field regions between electrodes of the same doping type. The ATLAS Insertable B-Layer project, to be implemented in the 2016 LHC Phase I upgrade, will consist of 25% 3D sensors [5].

The first full 3D sensors were fabricated at Stanford [10]. The fabrication process was developed further at SINTEF (Oslo, Norway) for larger-scale production [11], [12]. To simplify the fabrication process, double-sided processing was developed independently at both Fondazione Bruno Kessler (FBK) in Trento, Italy [7], and CNM-IBM [8].

The 3D sensors considered in this study are "Double-side Double-type Column" (3D-DDTC), from the batch ATLAS08, fabricated at FBK. In the original 3D-DDTC process at FBK, electrodes did not pass through the silicon bulk, resulting in low-field regions between the tip of the columns and the surface. In addition, calibration of the deep-reactive ion etching (DRIE) process to obtain the desired depth was difficult and prone to create differences in electrode overlap [9].

The sensors considered in this study are part of the second generation of FBK 3D-DDTC sensors, which are drilled from both sides of the wafer. The devices are electronically characterized before being placed in a beam at FNAL, both before and after proton irradiation. Similar studies of FBK 3D detectors have been done by the ATLAS collaboration [6], on sensors from a different wafer batch.

2. 3D Detectors

The sensors are fabricated on Float Zone p-type high-resistivity wafers, thickness 200 μm $\pm$ 20 μm. n+ (readout) electrodes are etched from the front side while p+ (ohmic) electrodes are etched from the back. All columns pass completely through the silicon bulk. The electrodes are hollow, with metal contact made to the wafer surface by small planar diffusion. Surface isolation of electrodes is accomplished by p-spray implantations on both wafer sides as shown in Figure 1.

These 3D devices house a standard edge region about 1 mm wide, with guard rings surrounding the active area. Double-sided sensors do not have an active edge, as that requires a support wafer which would make the backside inaccessible. The dead area has been decreased to 200μm or less in recent batches at FBK by implementing "slim-edge" technology [13]. More detailed information on 3D-DDTC can be found in [14], [15].

Each 3D sensor is read out electronically using the PSI46v2 read-out chip (ROC) [16]. The sensors are diced and bump-bonded to the ROC with indium bumps at SELEX in Italy. The ROC has 4160 read-out pixels arrayed as 52 columns $\times$ 80 rows, with pitch 150 μm and 100 μm, respectively.

Assembly is performed in a clean room at the P3MD lab at Purdue University. The assembly procedure is similar to that of the CMS forward pixel detector modules as described in [17]. Bump-bonded ROCs are glued and wire-bonded to a VHDI circuit, which in turn is wire-bonded to a fan-out board. The fan-out board and VHDI are glued to a base plate (Figure 2).

Three different 3D pixel configurations, 1E, 2E, and 4E, have been tested. "1E," "2E," and "4E" refer to the number of readout electrodes in each pixel. Each n+ electrode is surrounded by six p+ electrodes in the 1E configuration and four p+ electrodes in the 2E and 4E configurations (Figure 1). The inter-electrode distance for the 1E, 2E, and 4E configurations are 90 μm, 62.5 μm, and 45 μm, respectively. For 1E sensors, the inter-electrode distance refers to diagonal length from the center n+ electrode to the corner p+ electrodes, although there are p+ columns 50 μm from the n+ in the vertical direction to reduce the low-field regions between the n+ electrodes.
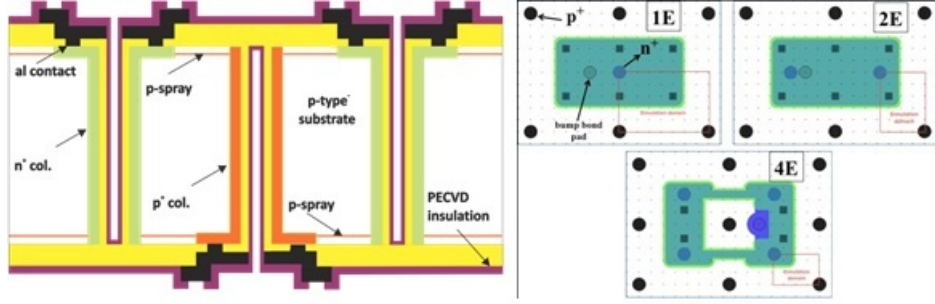
Figure 1: Left: 3D cross section. Electrodes are etched from either side and pass completely through the bulk. Right: Top-down view of FBK 1E, 2E, and 4E configurations.
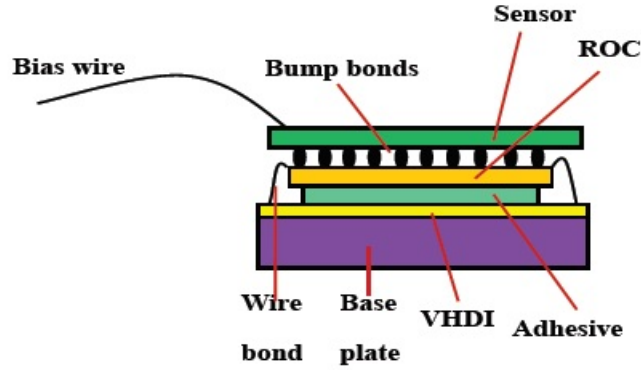

Figure 2: Artistic model of 3D assembly components. Each sensor is bump-bonded to a ROC, which is in turn connected to the DAQ system through a VHDI.

3. Sample preparation and lab setup

The experimental test stand consists of a PSI46 DAQ board with an adapter for 3D chips, connected to a PC. The DAQ board has an FPGA, a 12-bit ADC, and a 64 MB SDRAM buffer. The board and corresponding software were developed to qualify planar detectors using the PSI46v2 ROC [18], but was adapted for 3D use. An Agilent E3631A power supply provides voltage to the board. A Keithley 2410 source meter is used to bias the sensors and measure leakage current. For measurements that require cooling, the detector is placed inside a humidity-controlled cooling chamber.

3.1 Irradiation

Sensors are irradiated at the Los Alamos LANSCE facility. The average flux per macro-pulse for a 1 cm^2 sample is 2.33x10^{11} 800 MeV protons. The 1 MeV neutron equivalent NIEL damage factor for 800 MeV protons is 0.71 [19]. Obtained fluences are 7e14 n$_{eq}$/cm^2 and 3.5e15n$_{eq}$/cm^2. Due to laboratory procedure at Los Alamos, the sensors are left at room temperature for about one hour after irradiation before being transferred to a refrigerator at -20 °C. Other than this, no annealing is applied to the sensors after irradiation.

3.2 Test beam

The sensors are tested with 120 GeV protons at the Fermilab meson test beam facility. No magnetic field is applied. Devices under test (DUTs) are placed in pairs inside a telescope tracker (Figure 3). The trigger signal is provided by two PMTs coupled to scintillators downstream from the telescope.

The telescope consists of eight tracking planes – four 2x3 and four 2x4 FPIX plaquettes. Pixels in each chip are arranged in 52 columns with pitch 150 μm (local x-axis) by 80 rows with pitch 100 μm (local y-axis). The 2x3 and 2x4 planes are oriented perpendicular to one another and rotated 25 degrees about their local x-axes to increase charge sharing and improve the tracking resolution (Figure 4). More detailed information on the telescope can be found in [20].
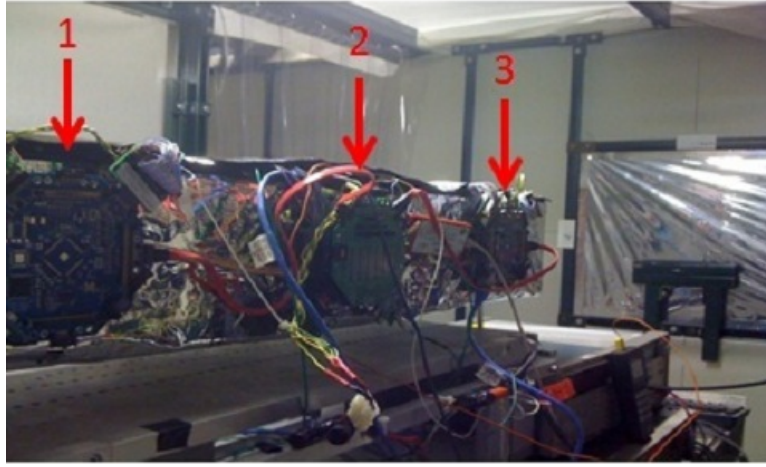

Figure 3: Photo of the telescope. There are three CAPTAN DAQ boards mounted on the telescope frame: one for the downstream (1), DUTs (2), and upstream (3).
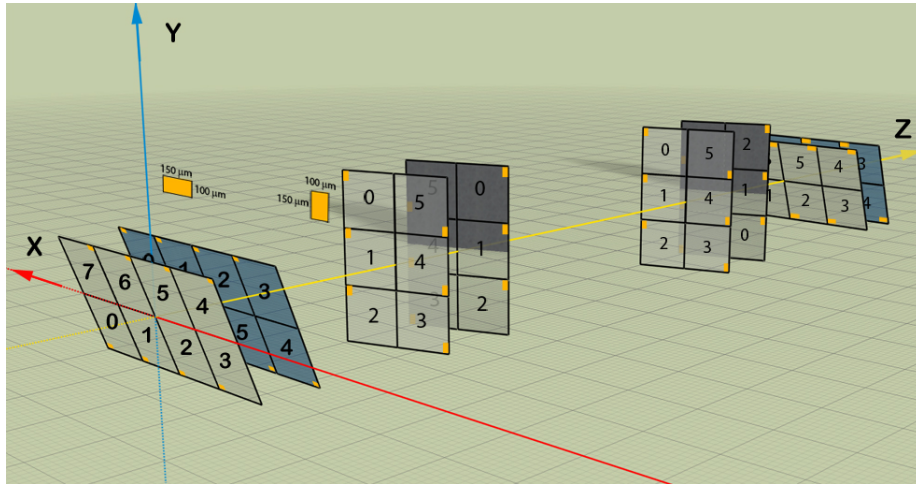

Figure 4: Geometrical layout of the telescope planes. The detectors are tilted at 25° with respect to the beam line (z-axis). The tilting is meant to improve resolution in the local plane y-coordinate, where pixel pitch is 100μm.

The 3D sensors are enclosed in a thermally isolated box with water-cooled Peltier elements for sensor cooling. The internal humidity and temperature of the box are monitored with a sensor mounted near the DUT. The box itself is mounted on top of a remotely controlled rotary stage inside the telescope enclosure. Temperature and angle are set remotely through a PC connection.

Data acquisition is controlled through CAPTAN, a DAQ system developed at FNAL [20]. CAPTAN employs a gigabit Ethernet connection which allows for remote control of the entire DAQ system from the test beam control room. The upstream telescope, downstream telescope, and DUTs are each attached to their own physical CAPTAN board. ROC voltages and settings are controlled through CAPTAN DAQ software.

Sensor charge collection, efficiency, and resolution are studied by independently varying bias, threshold, and angle. Each sensor's operational voltage is found with a bias scan before performing a readout threshold scan. Tracks are reconstructed for each event before determining efficiency and resolution. The telescope track error, measured by calculating the straight line best-fit errors of each event, is interpolated into the DUT resolution. It is determined to be approximately 7 μm in both local DUT coordinates (Figure 5).
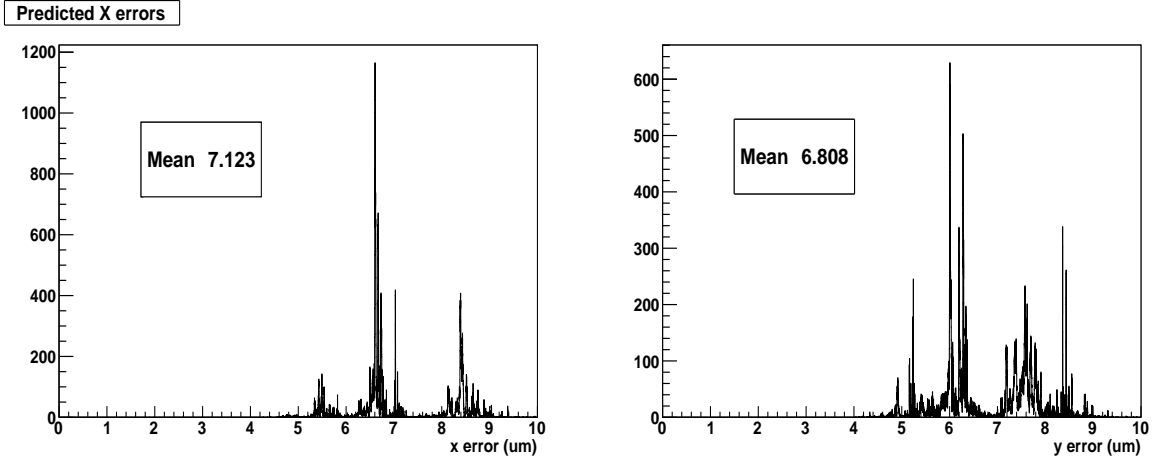
Figure 5: Telescope track errors in the local DUT x-coordinate (left) and y-coordinate (right).

4. Results and analysis

4.1 Simulation

TCAD simulations are carried out by solving continuity and Poisson equations simultaneously, including carrier drift, diffusion, generation, and recombination using Shockly-Read-Hall statistics and avalanche generation. A small characteristic portion of the pixel cell is simulated, and then scaled to the full size of the device.

A substrate thickness of 200 μm and electrode diameter of 12 μm is used. The substrate is p-type with a doping concentration of 7×10^{11} cm^{-3}, corresponding to a resistivity of ~ 20 k$\Omega \cdot$ cm. The doping concentration of all electrodes is assumed to be 5×10^{19} cm^{-3}. All parameters are representative of FBK technology.

The model used to simulate the devices is the University of Perugia proton radiation damage model for p-type FZ silicon, with modified parameters [23], [24]. The model consists of three trap levels with two acceptor levels and one donor. The two acceptor levels, positioned slightly above the midpoint of the band gap, increase leakage current, change the effective doping concentration, and trap excess electrons from the conduction band. The donor level is farther away from the midpoint and serves to trap excess holes from the valence band.

4.2 IV measurements

Leakage current (Figure 6) is measured before and after irradiation with a Keithley source meter. All devices experience breakdown between -20V and -40V bias. This is typical for FBK CMS 3D sensors [21]. Due to procedural variations and radiation damage it is difficult to determine the exact point of breakdown. Before and after irradiation, respectively, the instrument compliance is 99 μA and 505 μA; the IV is measured at room temperature and -20 °C.

There are notable discrepancies between lab and simulation results. The high leakage current and early breakdown in the real sensors are due to process-related defects. Fabrication-induced effects could not be incorporated into the simulations. These problems are now understood and have been improved in more recent batches [22].
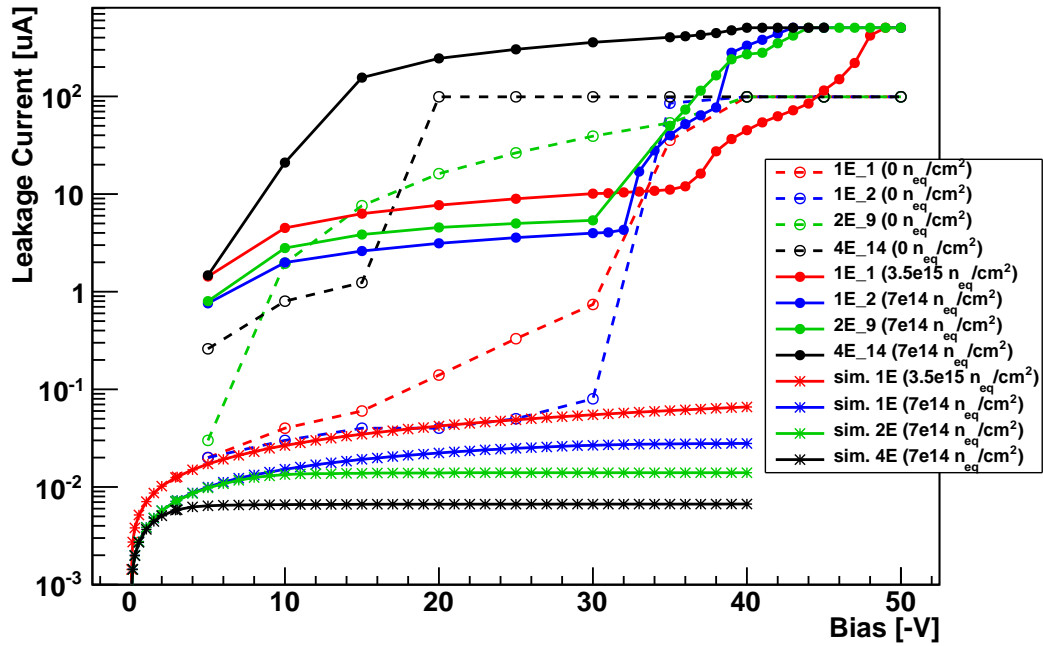

Figure 6: Leakage current before and after irradiation, with simulation results. Discrepancies between the lab data and simulation results are due to process-related surface defects, which are difficult to simulate.

4.3 Noise

Noise is determined by injection efficiency (S-curve) measurements, which are described in detail

in [11]. The readout efficiency for each pixel is found using internal charge injection via the chip, and the data is fitted with an S-curve. The width of the S-curve corresponds to the pixel noise. Noise measurements are taken at room temperature before irradiation, and -20 °C after irradiation. The tests are based on single measurements, with no averaging of S-curve results.

The sensor noise is related to the pixel capacitance (7). Capacitance (and thus noise) increases with radiation damage and closer electrode spacing, but decreases with reverse bias until full depletion, at which capacitance is a minimum. All of these behaviors are seen clearly in the 1E and 2E sensors. Noise increases by 20-30% in the 1Es and around 10% in the 2E. The 4E_14 does not experience the same noise behavior as the other sensors, though conclusions about this behavior are difficult to draw due to the low statistics and lack of cross-reference data.
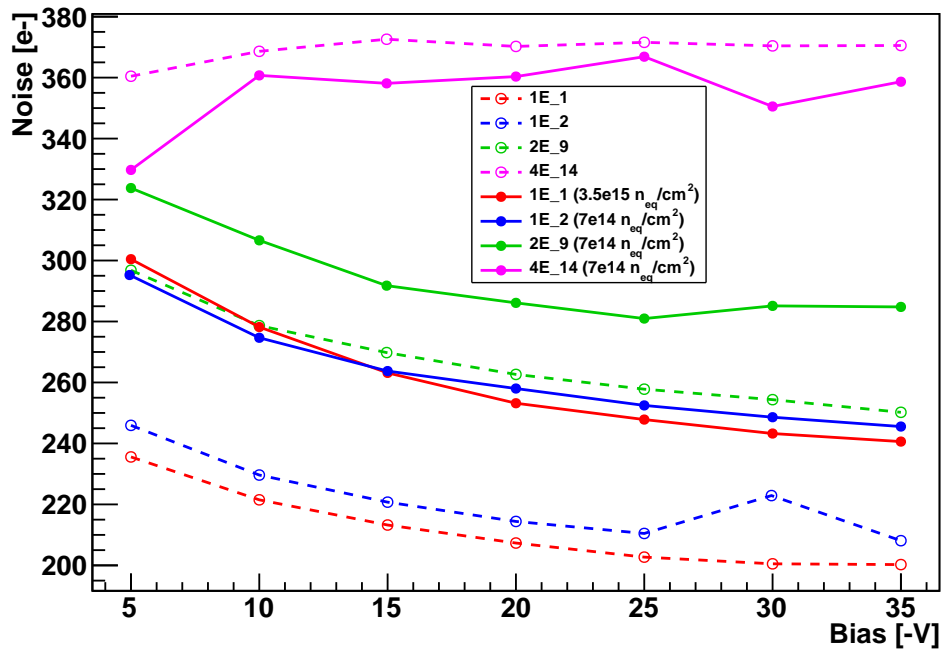

Figure 7: Noise before and after irradiation. Noise is related to pixel capacitance, which increases with radiation damage and closer electrode spacing, and decreases with reverse bias up to full depletion.

4.4 Test beam data analysis

Event data from the test beam is analyzed using software developed specifically for the Fermilab test beam. Charge is measured directly by the readout chip. Efficiency and resolution are calculated after iterative alignment of the telescope and DUTs. Both pre- and post-irradiation test beam data for a single 4E sensor is unavailable due to lack of measurements. Therefore pre-irradiation results are shown for the sensor 4E_12, while post-irradiation results are shown for the sensor 4E_14. Both sensors are from the same batch.

4.4.1 Charge collection

Charge collected for each run is determined by fitting the total single-pixel cluster charge distribution with a Gaussian convoluted Landau function and finding the MPV. Charge calibrations are performed under run conditions to determine the electron values. The 4E_14 was not calibrated and thus was not included in this section.

Figure 8 shows the collected charge plotted against reverse bias. Simulation results are included for comparison. Charge increases with bias and plateaus after depletion. Radiation damage effects are apparent in the charge losses and diminished plateau effect. Insufficient beam test data is available to provide a plot for the non-irradiated 2E sensor.

Figure 9 shows single-hit charge as a function of threshold. Threshold is given in DAC units which are negatively proportional to the threshold in electrons. Specific DAC-electron conversions are given at calibration thresholds in Table 1. Threshold trimming is not applied. Trimming is meant to make the threshold (in electrons) even across the entire sensor, as each pixel behaves differently. Here, thresholds are taken as the mean value across the sensor.

Relative charge losses at fixed thresholds, along with bias voltages, are listed in Table 2 for all sensors. Relative charge losses from both test beam studies and source tests are given.
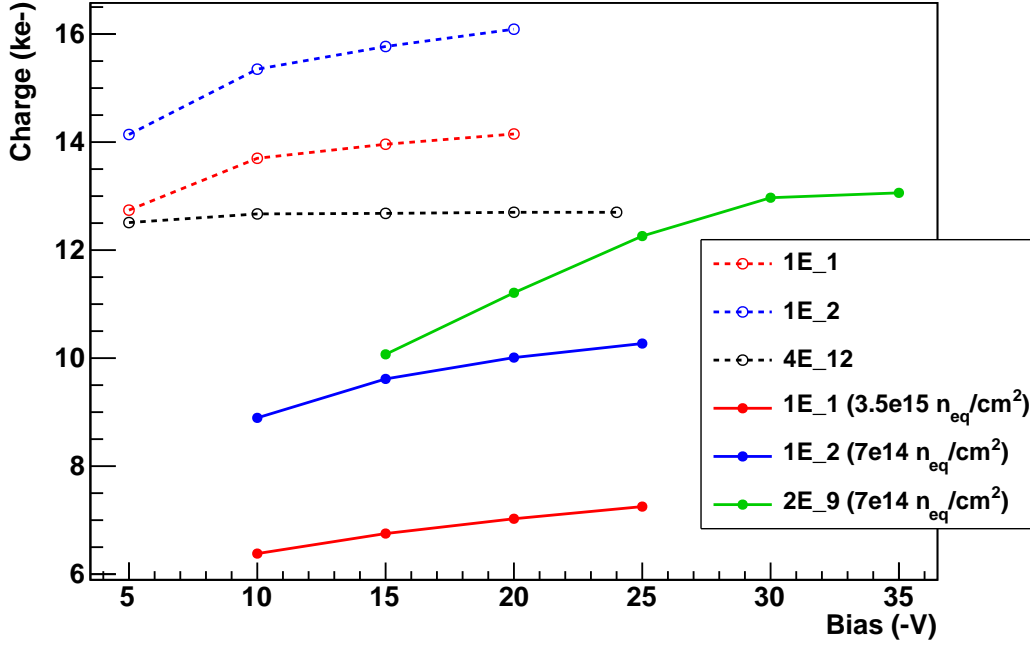

Figure 8: Charge (MPV) versus reverse bias voltage. The greatest loss after irradiation is seen in the highly irradiated 1E_1.

4.4.2 Tracking efficiency

An event's efficiency is equal to one if a hit is registered within one pixel width of a reconstructed track and zero otherwise. Efficiency is studied at normal beam incidence to the sensor plane.
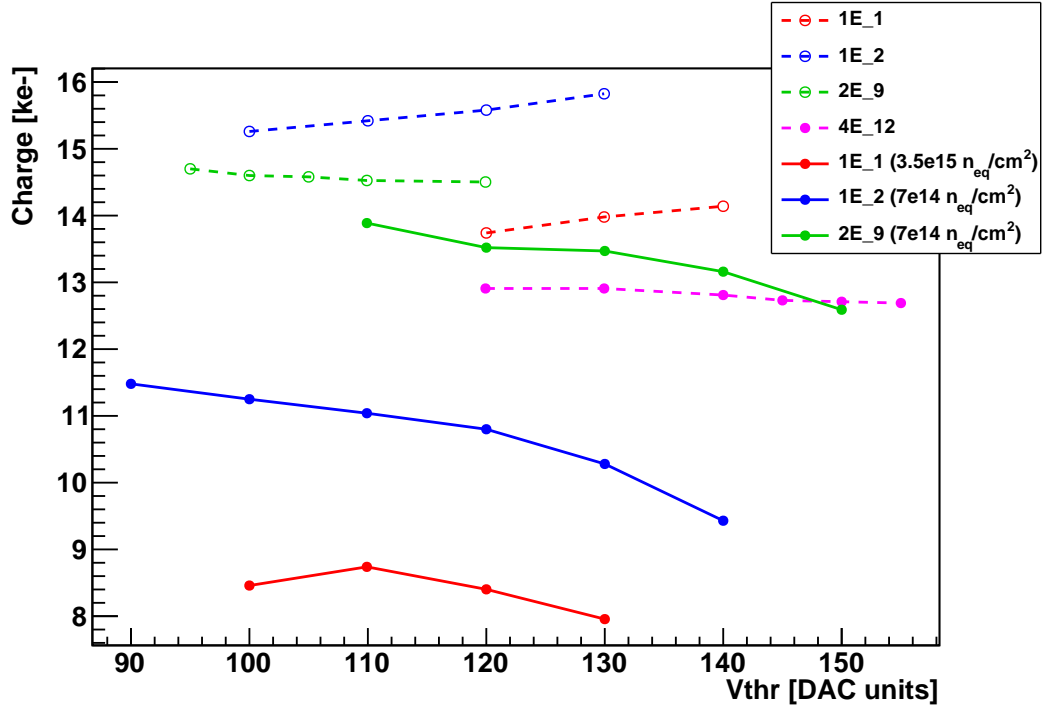
Figure 9: Charge (MPV) versus threshold in electronic DAC units. The greatest loss after irradiation is seen in the highly irradiated 1E_1. 2E_9 showed the least charge loss.

Sensor (fluence [n_{eq}/cm^2])	Vthr (DAC units)	Electron value
1E_1 (0)	130	4000
1E_2 (0)	130	5600
2E_9 (0)	110	6300
4E_12 (0)	140	6000
1E_1 (3.5e15)	130	4900
1E_2 (7e14)	130	4300
2E_9 (7e14)	130	5000
4E_14 (7e14)	130	6200

Table 1: Vthr-electron conversion at calibration thresholds.

Only events with one track are considered. The total sensor efficiency is determined by averaging the efficiency of all events in a run. The efficiency is strongly affected by the telescope track error, charge trapping, bias, and threshold. It is also affected to a lesser extent by the number of electrodes, which themselves are inefficient regions at normal beam incidence.

Figure 10 shows efficiency versus bias voltage. Operational bias voltages are determined from this data before scanning for optimum thresholds. Efficiency falls after approximately -30V due to breakdown in some sensors.

Figure 11 is a plot of tracking efficiency versus readout threshold. Efficiency rises as the threshold decreases, until eventually the noise becomes too great for the chip to distinguish be-

Sensor (fluence [n_{eq}/cm^2])	Bias (-V)	Threshold (e$^-$)	Charge (ke$^-$)	Charge loss
1E_1 (0)	15	4000	13.96	–
1E_2 (0)	15	5600	15.81	–
2E_9 (0)	5	6300	14.52	–
4E_12 (0)	15	6000	12.81	–
1E_1 (3.5e15)	35/40	4900	7.96	43%
1E_2 (7e14)	25	4300	10.28	35%
2E_9 (7e14)	30	5000	13.47	7%
4E_14 (7e14)	15	6200	no calib.	n/a

Table 2: Charge collection at constant thresholds, before and after irradiation. Relative charge loss is lowest for the 2E_9 and significantly greater for both 1Es.

tween real hits and noise. At this point the sensor sees an efficiency drop. Radiation-induced traps also degrade the signal, causing a drop in tracking efficiency due to the decreased signal-to-noise ratio. Table 3 lists the maximum efficiency achieved in each sensor and the relative loss after irradiation.
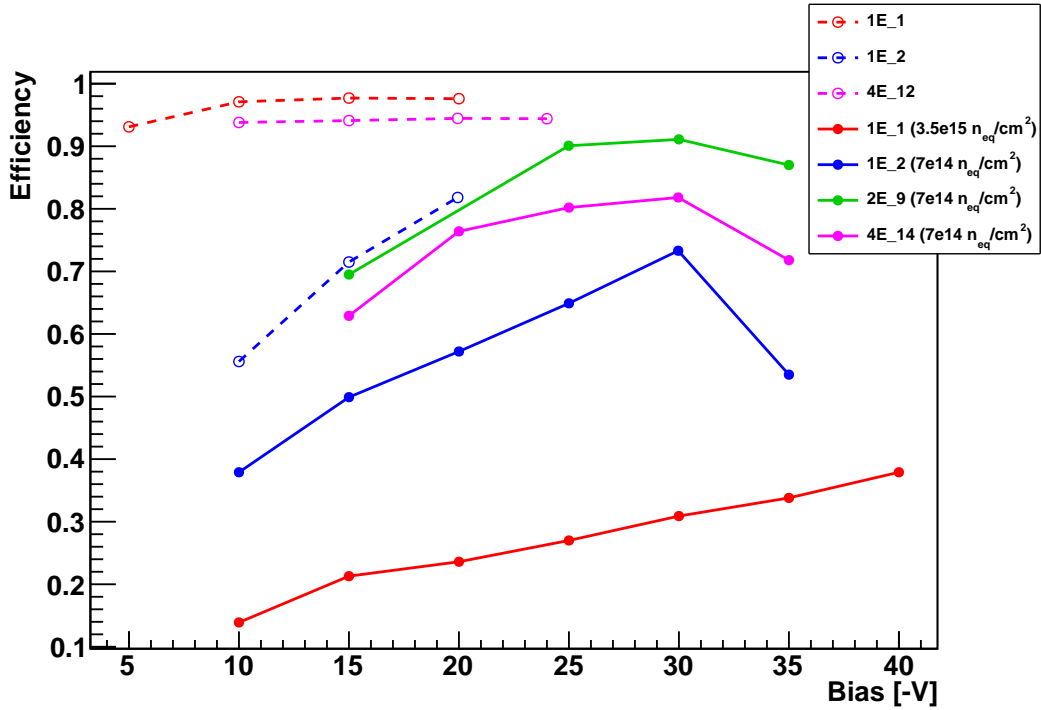

Figure 10: Tracking efficiency versus bias. Efficiency drops at biases close to breakdown.

Figure 12 shows cell efficiency (tracking efficiency over a single pixel area) versus angle for each sensor after irradiation. Radiation level has a significant effect on efficiency far away from the readout – the 1E_2 (7e14 n_{eq}/cm^2) is approximately 35-40% efficient at the corners and the left
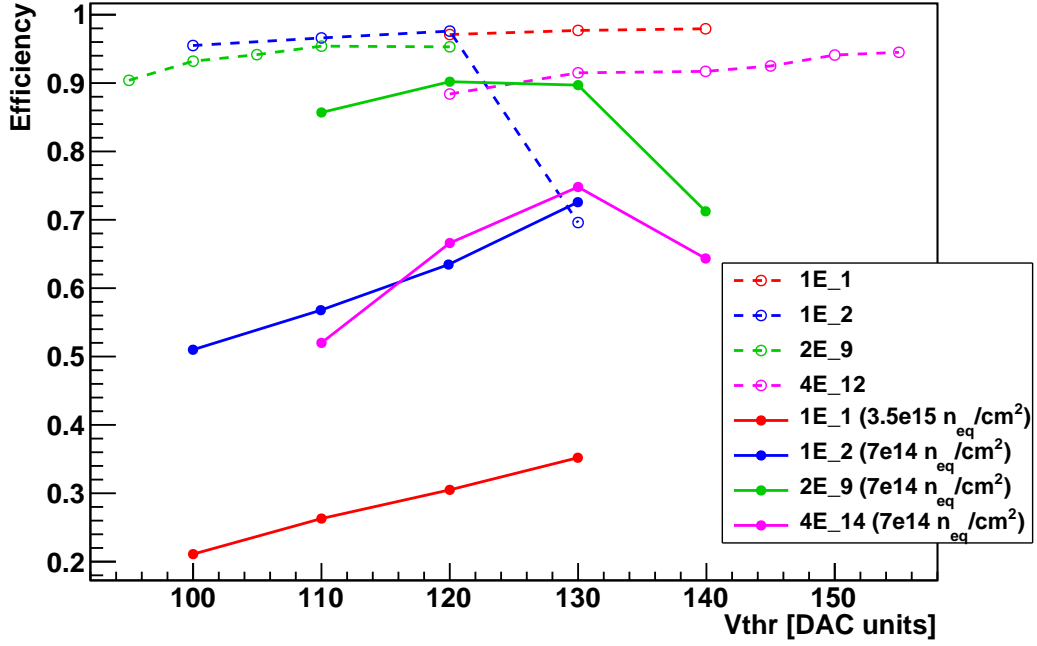
Figure 11: Tracking efficiency versus threshold. In some cases, the efficiency falls at low threshold due to low signal-to-noise ratio.

Sensor (fluence [n_{eq}/cm^2])	Maximum efficiency	Efficiency loss
1E_1 (0)	97.8%	–
1E_2 (0)	97.6%	–
2E_9 (0)	95.4%	–
4E_12 (0)	94.5%	–
1E_1 (3.5e15)	37.9%	59.9%
1E_2 (7e14)	73.1%	24.5%
2E_9 (7e14)	91.1%	4.3%
4E_14 (7e14)	81.7%	n/a

Table 3: Maximum tracking efficiency achieved before and after irradiation. Efficiency loss is greatest in the highly irradiated 1E_1 and smallest in the 2E_9.

and right pixel edges, while in the same regions the 1E_1 (3.5e15 n_{eq}/cm^2) is almost completely inefficient. The 1E_2 provides a good example of how angle affects charge sharing. At normal incidence, particles are detected almost exclusively in a circular area around the readout electrode. As the sensor is tilted in the local y-direction, more charge is detected along the top and bottom edges where charge sharing is prominent. In the case of the 4E_14, the lack of charge calibration lowers the efficiency.
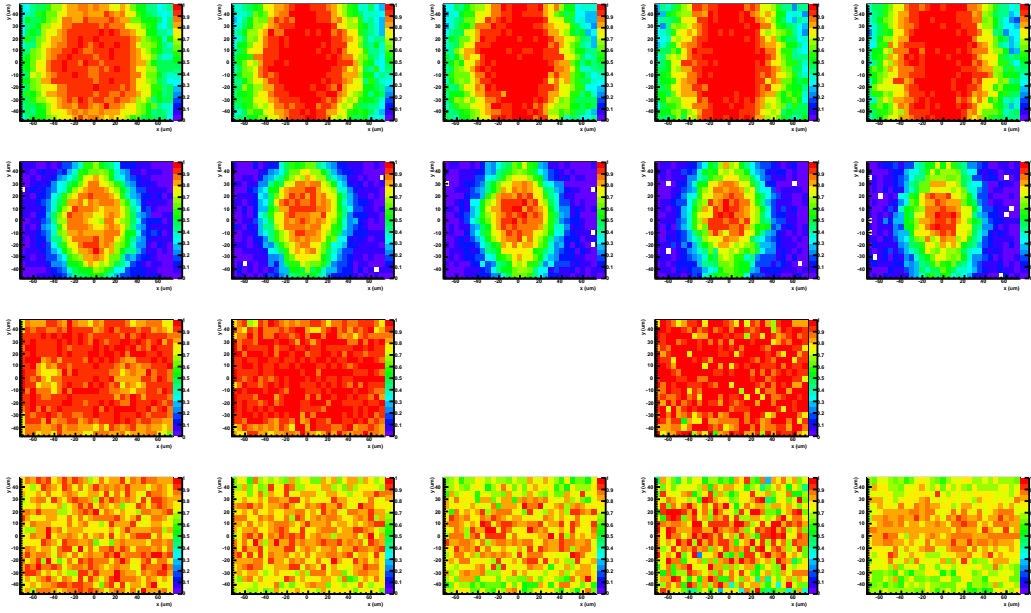
Figure 12: Cell efficiency versus angle. Top to bottom: 1E_2 (7e14 n_{eq}/cm^2), 1E_1 (3.5e15 n_{eq}/cm^2), 2E_9 (7e14 n_{eq}/cm^2), 4E_14(7e14 n_{eq}/cm^2). Left to right: 0, 10, 15, 20, 25 degrees angle of incidence. Two runs for the 2E had errors and are not shown.

4.4.3 Position resolution

Track residuals are calculated as the distance between the predicted (from track reconstruction) and measured positions of a cluster, in either the local x or y direction. The residuals are fitted with a Gaussian; the overall sensor resolution is determined from the sigma of the fit (Figure 13). For single-hit clusters the residual is the width of the pixel (100 μm in y and 150 μm in x). Better resolution is obtained when charge is shared between pixels. In the CMS barrel, this is achieved through a combination of detector tilt and a 4 T magnetic field. The test beam DUTs are tilted to various angles to emulate these effects.

Residuals for irradiated sensors can be improved through charge asymmetry studies. Charge asymmetry is a plot of collected charge versus x/y cluster position, averaged over each pixel. This is done on the first DUT alignment. Residuals are improved by reiterating the alignment procedure and using the measured charge to determine cluster positions directly from the asymmetry plot. This will be implemented in future 3D studies.

5. Summary and Conclusions

3D tracking detectors are a promising radiation-hard candidate to replace planar detectors in the HL-LHC. The Phase II upgrade will expose the innermost barrel sensors to a fluence of approximately 10^{16} n_{eq}/cm^2. Electrical and beam tests were performed for FBK ATLAS08 3D detectors before and after irradiation. The detectors were assembled and wired at the P3MD lab at Purdue University, and bump-bonded at SELEX, Italy. Three of the detectors were irradiated to 7e14 n_{eq}/cm^2, and one to 3.5e15 n_{eq}/cm^2. Radiation damage effects are demonstrated with regards to

1E_2 ($7 \times 10^{14}\ n_{eq}/cm^2$)

Mean	5.951
RMS	25.61
Constant	771.3
Mean	6.708
Sigma	17.8

y (um)

2E_9 ($7 \times 10^{14}\ n_{eq}/cm^2$)

Mean	0.7092
RMS	19.23
Constant	236
Mean	-0.09775
Sigma	12.56

y (um)

1E_1 ($3.5 \times 10^{15}\ n_{eq}/cm^2$)

Mean	-4.025
RMS	33.41
Constant	119.1
Mean	-2.645
Sigma	18.29

y (um)

4E_14 ($7 \times 10^{14}\ n_{eq}/cm^2$)

Mean	0.09809
RMS	26.77
Constant	320.1
Mean	0.1474
Sigma	20.79

y (um)
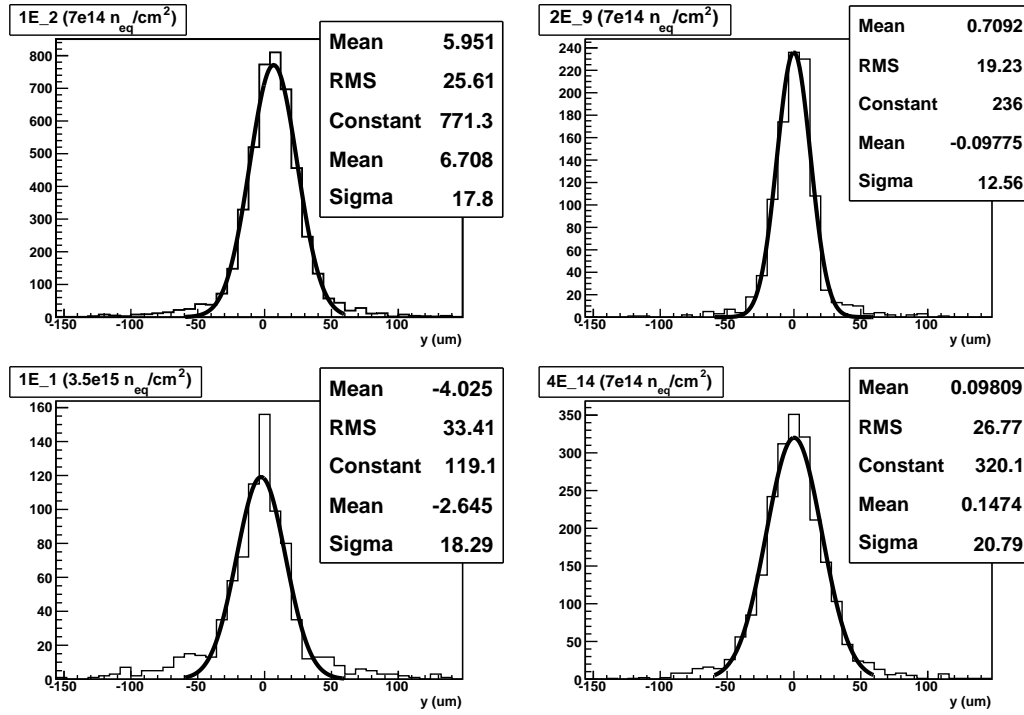
Figure 13: Irradiated residual plots fit with a Gaussian. Top left: 1E_2 (17.8 μm); top right: 2E_9 (12.56 μm); bottom left: 1E_1 (18.29 μm); bottom right: 4E_14 (20.79 μm). The 1E_1 provided low statistics, and the 4E_14 was not calibrated.

charge collection, efficiency, and resolution of the particle tracks in beam tests, as well as leakage current and pixel noise. After irradiation, the 2E showed the least degradation of charge and efficiency. The sensor 4E_14 was not calibrated and thus further tests are necessary to study 4E post-irradiation performance. Lab and test beam studies are ongoing for more recent batches from FBK, with improved fabrication processes.

Acknowledgments

References

[1] Silicon Strip Detectors for the ATLAS HL-LHC Upgrade, Physics Procedia, Volume 37, 2012, 915-922, ISSN 1875-3892.

[2] Caminada, Lea, *Recent Developments of HEP Pixel Detector Readout Chips*, Physics Procedia, 1644-1653 (2012), 37, ISSN 1875-3892.

[3] Paula Collins, *Semiconductor detectors for high-luminosity environments*, Nucl. Inst. and Meth. A, 581 (2007) 38.

[4] S. I. Parker et al., *3D - A proposed new architecture for solid-state radiation detectors*, Nucl. Instr. and Meth. A 395 (1997) p. 328.

[5] ATLAS Collaboration, *ATLAS Insertable B-Layer Technical Design Report Addendum*, CERN, Geneva, 2012.

[6] A. Micelli et al., *3D-FBK pixel sensors: Recent beam tests results with irradiated devices*, Nucl. Inst. and Meth. A, 650 (2011) p. 150.

[7] A. Zoboli et al., *Double-sided, Double-Type Column 3-D Detectors: Design, Fabrication and Technology Evaluation*, IEEE Trans. Nucl. Sci., vol. 55, no. 5, pp. 2775-2784, 2008.

[8] G. Pellegrini et al., *First double-sided 3-D detectors fabricated at CNM-IMB*, Nucl. Instr. and Meth. A 592 (2008) 38.

[9] A. La Rosa et al., *Characterization of proton irradiated 3D-DDTC pixel sensor prototypes fabricated at FBK*, Nucl. Instr. and Meth. A 681 (2012) pp. 25-33.

[10] C. Kenney et al., *Silicon detectors with 3-D electrode arrays: fabrication and initial test results*, IEEE Trans. Nucl. Sci., vol. 46, no. 4, pp. 1224-1236, 1999.

[11] O. Koybasi et al., *Electrical Characterization and Preliminary Beam Test Results of 3D Silicon CMS Pixel Detectors*, IEEE Trans. Nucl. Sci., vol. 55, no. 5, pp. 2775-2784, 2008.

[12] T.E. Hansen et al., *First fabrication of full 3D-detectors at SINTEF*, 2009 JINST 4 P03010.

[13] M. Povoli et al., *Slim edges in double-sided silicon 3D detectors*, 2012 JINST 7 C01015.

[14] G.-F. Dalla Betta et al., *Development of modified 3D detectors at FBK*, 2010 IEEE NSS, Conference record paper N15-3.

[15] E. Vianello et al., *Optimization of double-side 3D detector technology for first production at FBK*, 2011 IEEE NSS, Conference record paper N10-6.

[16] W. Erdmann, *The 0.25 μm front-end for the CMS pixel detector*, Nucl. Instr. and Meth. A 549 (2005) 153.

[17] O. Koybasi et al., *Assembly and qualification procedures of CMS forward pixel detector modules*, Nucl. Instr. and Meth. A 638 (2011) 55.

[18] A. Starodumov et al., *Qualification procedures of the CMS pixel barrel modules*, Nucl. Instr. and Meth. A 565 (2006) 67.

[19] A. Vasilescu and G. Lindstroem, *Displacement damage in silicon*, Online compilation, http://polzope.in2p3.fr:8081/ATF2/collected-information/displacement-damage-in-silicon-from-unno-san-kek/.

[20] R. Rivera et al., *A Telescope Using CMS PSI46 Pixels and the CAPTAN for Acquisition and Control over Gigabit Ethernet*, 2009 IEEE NSS, Conference record paper.

[21] E. Alagoz et al., *Simulation and laboratory test results of 3D CMS pixel detectors for HL-LHC*, 2012 JINST 7 P08023.

[22] M. Obertino et al., *3D-FBK pixel sensors with CMS readout: First test results*, Nucl. Instr. and Meth. A Proof (2012).

[23] M. Petasecca et al., *Numerical Simulation of Radiation Damage Effects in p-Type and n-Type FZ Silicon Detectors*, Nuclear Science, IEEE Transactions on, vol.53, no.5, pp.2971-2976, Oct. 2006

[24] D. Pennicard et al., *Simulations of radiation-damaged 3D detectors for the Super-LHC*, Nucl. Instr. and Meth. A 592 (2008) 16.

[25] P. Trub, *CMS pixel module qualification and Monte-Carlo study of $H \to \tau^- \tau^- \to l^+ l^- E_T$*, Ph.D. dissertation, ETH Zurich, Zurich, Switzerland, 2008.